Theoretical investigation of the OH-initiated atmospheric degradation mechanism of CX_2=CHX (X = H, F, Cl) by advanced quantum chemical and transition state theory methods.

Nadjib Rais[a,b], Zoi Salta[a*] and Nicola Tasinato[a]

[a] *Scuola Normale Superiore, Piazza dei Cavalieri 7, I-56126, Pisa, Italy*

[b] *IUSS Scuola Universitaria Superiore, Piazza della Vittoria 15, I-27100, Pavia, Italy*

ABSTRACT: Halogenated olefins are anthropogenic compounds with many industrial applications but at the same time raising many environmental and health concerns. Gas-phase electrophilic addition of the OH radical to the olefinic C=C bond represents the primary sink for these chemicals in the atmosphere, with the degree and type of halogenation playing a significant role in their overall reactivity. In this work, we present a theoretical investigation of the reaction mechanisms and kinetics for the reactions between the OH radical and CH_2=CH_2 (Ethylene, ETH), CF_2=CHF (Trifluoroethylene, TFE) and CCl_2=CHCl (Trichloroethylene, TCE), simulated by state-of-the-art protocols and methods, with the aim of providing a detailed interpretation of the available experimental results, as well as new data of relevance to tropospheric chemistry. Specifically, potential energy surfaces (PESs) are obtained by the jun-Cheap (jChS) composite scheme, whereas temperature and pressure dependent rate coefficients and product distributions in the 100 – 600 K temperature range are calculated within the Rice–Ramsperger–Kassel–Marcus/Master Equation (RRKM/ME) framework. The rates for barrierless channels are obtained from Variable Reaction Coordinate-Variational Transition State Theory (VRC-VTST) combined with two transition state model. While the reactions with ETH and TFE proceed mainly via the formation of addition adducts at P = 1 atm and T = 298 K, the dominant channel for TCE is the Cl-elimination reaction. Global rate constants for the two halogenated olefins, TFE and TCE, are found to be pressure-independent, contrary to the case of ETH. The computed rate constants, as well as their temperature and pressure dependence, are in remarkable agreement with the available experimental data, and they are used to derive atmospheric lifetimes (τ) for both TFE and TCE as a function of altitude (h) in the atmosphere, by taking into account variations in the rate coefficients ($k\ (T, P)$) and [OH] concentration.

Keywords: HFO-1123, trichloroethylene, rate constants, product distributions, atmospheric lifetimes

***Corresponding author:** Dr. Zoi Salta, Scuola Normale Superiore, piazza dei Cavalieri 7, 56126 Pisa, Italy, E-mail: Zoi.Salta@sns.it

1. INTRODUCTION

In recent years, air pollution has been recognized as a worldwide health issue, despite the adoption of various control policies and measures.[1] The challenges of overpopulation, rapid urbanization, and large-scale industrialization contribute to the escalation of primary and secondary air pollutants which are responsible for the rapid decline of the environment and pose serious risks to human health. Their release in the atmosphere, mainly due to anthropogenic activity, affects the Earth's climate by contributing to ozone depletion and global warming.[2,3] A large portion of those hazardous substances comes from the oxidation reactions of halogenated organic compounds and, despite the increasing efforts by researchers from different scientific fields to simulate and predict their evolution and final fate, there is still a great uncertainty in connecting field measurement observations to laboratory experiments.[4,5] For that reason, predictions and/or verifications coming from theoretical simulations are often deemed necessary in order to fill existing gaps of atmospheric models.

One of the most recent examples was reported in 2019 in France, when trichloroethylene (CCl_2=CHCl, TCE), a chemical already connected to a great number of health problems, [6,7]was detected in a local household in concentrations almost 800 times above the legally accepted limit. TCE was initially synthesized in 1864 and commercially produced in the 1920s. Its distinctive characteristics (high volatility, strong solvent capacity) has led over the years to a large amount of industrial, commercial, military, and medical uses, one of them being the production of other chlorinated compounds. Previous experimental and theoretical work has shown that the major products of the atmospheric oxidation of TCE are phosgene (CCl_2O), dichloroacetyl chloride ($CHCl_2CClO$), formyl chloride (CHClO), and most importantly Cl atoms.[8–10] Despite its importance, there have been only two studies that examined theoretically the reaction mechanism between CCl_2=CHCl and OH. Initially, Tichenor et al.[11] concluded that at room temperature, the primary reaction is adduct stabilization, while Cl-elimination occurs at much higher temperatures (1000 K). Later on, Christiansen and Francisco[10] provided a general atmospheric oxidation scheme, studying the Cl atom's role in the reaction and its effect on overall kinetics. However, none of the above studies provided a comprehensive analysis of the mechanistic and kinetic details of this specific reaction.

Trifluoroethylene (CF_2=CHF, TFE) on the other hand (also known as HFO-1123), due to its reduced global warming potential (GWP)[12] and short atmospheric lifetime, is supposed to

be environmentally more friendly and industries have already started using it as an ingredient in refrigerant blends.[13] For that reason, however, the scientific community has started to show increased interest in reaching a deeper understanding not only of the species' properties, but also of its atmospheric reactivity and final fate.[14-19] In previous studies related to the environmental impacts of fluorinated ethenes, the temperature dependencies of the reaction rate constants of CF_2=CHF with OH radicals have been reported by two groups using the absolute[15] and relative rate methods.[14] The only existing theoretical study on the reaction was provided by Snitsiriwat et al.[17] who performed the kinetic analysis using conventional transition state theory and Quantum Rice-Ramsperger-Kassel (QRRK) master equation calculations. The authors concluded that stabilization of the initial adducts along with HF elimination are the important reaction pathways under high pressure and low temperature conditions. Their results, which were found to be in good agreement with the experimental ones at room temperature, cannot however be extended to tropospheric conditions.

Based on those premises, the current study aims to investigate by means of state-of-the-art quantum chemical methods the reaction mechanism of the OH-initiated degradation of TFE and TCE and to predict the rate constants for the different competing reaction channels, which determine, in turn, atmospheric lifetime vertical profiles and the distribution of the different first-generation products. [20,21] For the purpose, reliable computational thermochemical and kinetics methods are required to explore reactive potential energy surfaces (PES), derive accurate thermochemical properties, global rate constants and product distributions. The reliability of the adopted protocol is first validated by evaluating the thermochemistry and kinetics details of the widely studied reaction between ethylene (ETH) and OH, providing at the same time, new data concerning the product distributions of the reaction at tropospheric relevant temperatures. In addition to rate constants, product distributions and atmospheric lifetimes, the effect of different halogen substitution on the progress of the reaction is analyzed in detail.

2. COMPUTATIONAL METHODS

2.1. Electronic Structure Methods

One of the fundamental steps necessary for performing reliable kinetic studies is the accurate characterization of all the stationary points found in the potential energy surface (PES) of a reaction under investigation. In this work, the exploration of the PESs that will be presented

was initially evaluated with the use of the AutoMeKin (AMK) computer code, [22–24] which combines molecular dynamics (MD) simulations, post-processing, and careful selection of the transition state (TS) molecular structures obtained from the MD simulations, in order to create possible connecting paths of a specific reaction. After a careful filtering of all the plausible reaction mechanisms provided by AMK, double-hybrid functionals in conjunction with basis sets of at least triple-ζ quality, which are known to represent a remarkable compromise between accuracy and computational cost,[18,21,25,26] were used to characterize the structural and vibrational parameters of all species ruling the PESs. Specifically, equilibrium geometries and harmonic vibrational frequencies of the stationary points were calculated with the double hybrid rev-DSD-PBEP86 density functional theory[27], that was augmented by DFT-D3 dispersion with Becke-Johnson (BJ) damping, [28,29] in conjunction with the partially augmented jun-cc-pV(T+*d*)Z[30] basis set, which includes an additional set of polarization *d* functions required to achieve a consistent description of second-row elements. [31–33]

In a following step, the energetics of all stationary points were refined by exploiting the parameter-free composite scheme, "jun-cheap" (jChS), [34,35] that has demonstrated a sub-chemical accuracy for a number of reaction energies and barriers. [36–40] In brief, the jChS composite scheme starts from the CCSD(T)/jun-cc-pV(T+*d)*Z energy within the frozen-core approximation that is improved by the extrapolation to the complete basis set limit (CBS) [41] and the inclusion of core-valence correlation (CV) performed using the Møller-Plesset second-order perturbation theory[42] (readers are referred to the specific literature for a complete account).

The MD calculations in AutoMeKin were performed using the semi-empirical PM7 method[42] as implemented in the MOPAC software, [44] the DFT calculations were performed with Gaussian16, Revision C.01, [45] and all the steps of the jChS composite scheme were done with the MOLPRO[46] computer program.

2.2. Kinetic models

2.2.1. Barrierless OH-addition

The addition of the OH radical to olefins is a well-known radical-molecule reaction that involves at least two transition states, namely a submerged inner transition state where the chemical bond is starting to form (short-range), and an outer transition state corresponding to

the formation of a van der Waals complex (long-range). This behavior, usually referred to as transition state switching or channel switching, may lead to a dominant long-range kinetic bottleneck at low temperatures. [47] An accurate determination of the rate constant for the reactions under study requires a proper account of the sequential effect of the two bottlenecks, which has been obtained in the present paper by the two transition state model[48,49] coupled with Variable Reaction Coordinate-Variational Transition State Theory (VRC-VTST) with a multifaceted dividing surface.[50,51] The Monte Carlo sampling was performed using the spin-unrestricted density functional method M08-HX[52] in conjunction with the MG3S basis set.[53] This level of theory choice was validated against jChS. Further details regarding this benchmark and the VRC-VTST setup are provided in the Supporting Information of this study.

2.2.2. H-abstraction pathways

Rate constants for the H-abstraction pathways were calculated by using variational transition-state theory (VTST)[54] employing a dual-level strategy[55,56] that combines conventional transition state theory results obtained at the jChS level with recrossing and tunneling (small-curvature tunneling) effects calculated using the M08-HX functional. The anharmonicity of the CCOH torsional mode was taken into account by means of the MSTor model,[57] whereas the anharmonicity for the remaining modes was taken into account by employing a purposely determined scaling factor. The latter was obtained as the ratio between anharmonic ZPVEs issuing from hybrid degeneracy corrected second order perturbation theory (HDCPT2),[58] to the harmonic value and was applied to scale the harmonic ZPVE for all the points along the reaction path. All VRC-VTST and VTST calculations were performed using Polyrate 2017C[59] and Gaussrate 17B[60] codes.

2.2.3. Temperature- and Pressure-dependence

The temperature- and pressure-dependence of the phenomenological rate coefficients was calculated by solving the Energy-Grained Master Equation (EGME), based on the chemically significant eigenvalue (CSE) method, as implemented in the MESS software.[61] For elementary steps governed by distinct saddle points, conventional rigid-rotor harmonic-oscillator (RRHO) transition state theory with asymmetric Eckart tunneling[62] was employed. Instead, rate constants for barrierless elementary reactions were computed by employing VRC-VTST.

An exponential downward model was used for the collision energy transfer probability, with $\langle \Delta E_{down} \rangle = 260(T/300)^{0.9}$ cm^{-1} and 300 cm^{-1} for the reactive systems $CH_2=CH_2$ + OH, $CF_2=CHF$ + OH and $CCl_2=CHCl$ + OH. The collision rate for energy transfer collisions was calculated using a Lennard-Jones model, with the LJ parameters obtained from the RMG database[63].

3. Results and Discussion

For the three reactions considered, namely the OH-initiated degradation of $CH_2=CH_2$, $CF_2=CHF$ and $CCl_2=CHCl$, addition, abstraction and isomerization processes have been investigated, starting with the prototypical ethylene system, which has allowed a careful validation of the accuracy of the adopted quantum chemical procedure. Details of the reaction pathways, global rate constants as well as product distributions for the OH-initiated atmospheric degradation of $CH_2=CH_2$ (ETH), are presented in section 3.1. Subsequently, the thermodynamic and kinetic evaluation for the $CF_2=CHF$ (TFE) and $CCl_2=CHCl$ (TCE) are presented in the subsections 3.2 and 3.3, respectively. Finally, subsections 3.4 and 3.5 provide some general reactivity patterns and atmospheric implications, respectively, for all three systems investigated in the current study.

3.1. $CH_2=CH_2$ + OH

3.1.1. Thermodynamic evaluation

The reaction between $CH_2=CH_2$ and OH has already been deeply studied over the years both experimentally[64–69] and theoretically, [48,70–73] serving more than once as a benchmark for exploring a variety of either similar reactions of unsaturated olefins or diverse theoretical techniques. As already pointed out, it will serve the same purpose also in the current study. The full PES for the $CH_2=CH_2$ + OH reactive system as calculated at the jChS level of theory is presented in Figure 1. The reaction initiates either with the formation of a pre-reactive addition complex (PRCadd) that lies 1.6 kcal mol^{-1} below the reactants at 0 K, or with a direct hydrogen abstraction (through TSabs) to form water and vinyl radicals (P1). PRCadd can further proceed via a submerged transition state (TSadd) to forming the very stable 2-hydroxyethyl radical (IM1). IM1 can, of course, further isomerize via [1,3] and [1,2] H-shifts to the ethoxy radical

(IM2) or to the 1-hydroxyethyl radical (IM3), respectively, but both processes involve high energy barriers (TS1 and TS2). The second set of products (P2), vinyl alcohol (CH_2CHOH) and H atoms, comes from the decomposition of IM1, after overcoming TS3. On the other hand, IM2 can isomerize (through TS4) to IM3, or decompose (through TS5) to formaldehyde and the methyl radical (P4: $CH_2O + CH_3$). Finally, IM3 can produce H atoms and form either the vinyl alcohol (P2: CH_2CHOH) through TS8 or acetaldehyde (P3:CH_3CHO) through TS7.

As already mentioned, several quantum chemical studies are available in the literature for the prototypical reaction between OH and ethylene, [64,70,72,73] with the most detailed and accurate analyses being probably those performed in 2006 by Senosiain et al. [70] and Cleary et al. [64] Inspection of the different results summarized in Table 1 shows that all the computational approaches provide comparable trends, and, in particular, the jChS relative energies computed in this work are in good agreement (<1 kcal mol^{-1}) with the other high-level ones of refs. 64 and 70.

Table 1. Relative energies Δ(E+ZPE) of the stationary points present in the PES of the $CH_2=CH_2$ + OH reaction. Values are given in kcal mol^{-1}.

	[a] Senosian et al. [70]	[b] Cleary et al. [64]	[c] Ali and Barker [72]	[d] This work
R1: $CH_2=CH_2$ + OH	0.0	0.0	0.0	0.0
PRCadd	-1.9	-1.8	-1.9	-1.6
IM1 (CH_2CH2OH)	-26.2	-27.5	-26.5	-26.6
IM2 (CH_3CH_2O)	-22.8	-25.4	-23.7	-22.7
IM3 (CH_3CHOH)	-32.7	-	-32.8	-33.6
TSabs (R1 → P1)	4.9	7.3	4.7	5.3
TSadd (R1 → IM1)	0.2	-0.8	-0.7	-0.1
TS1 (IM1 → IM2)	5.7	3.3	5.4	5.8
TS2 (IM1 → IM3)	12.1	-	12.8	11.9
TS3 (IM1 → P2)	6.9	-	7.6	6.7
TS4 (IM2 → IM3)	4.4	-	4.4	4.3
TS5 (IM2 → P4)	-5.5	-7.4	-5.8	-5.4
TS6 (IM2 → P3)	-1.5	-3.1	-1.8	-1.5
TS7 (IM3 → P3)	2.4	-	2.6	2.4
TS8 (IM3 → P2)	3.7	-	4.2	3.5
P1 ($CH_2CH + H_2O$)	-8.3	-8.0	-7.3	-8.4
P2 (CH_2CHOH + H)	1.0	-	3.6	1.1
P3 (CH_3CHO + H)	-8.8	-9.8	-8.1	-8.5
P4 ($CH_2O + CH_3$)	-13.1	-13.3	-12.7	-12.9

[a] RQCIT//UQCISD/6-311++G(d,p); [b] CBS-APNO//BH&HLYP/6-311+G(3df,2p); [c] CCSD(T)/aug-cc-pVTZ//BHandHLYP/aug-cc-pVTZ; [d] jChS//rev-DSD-PBEP86-D3(BJ)/jun-cc-pV(T+*d*)Z.

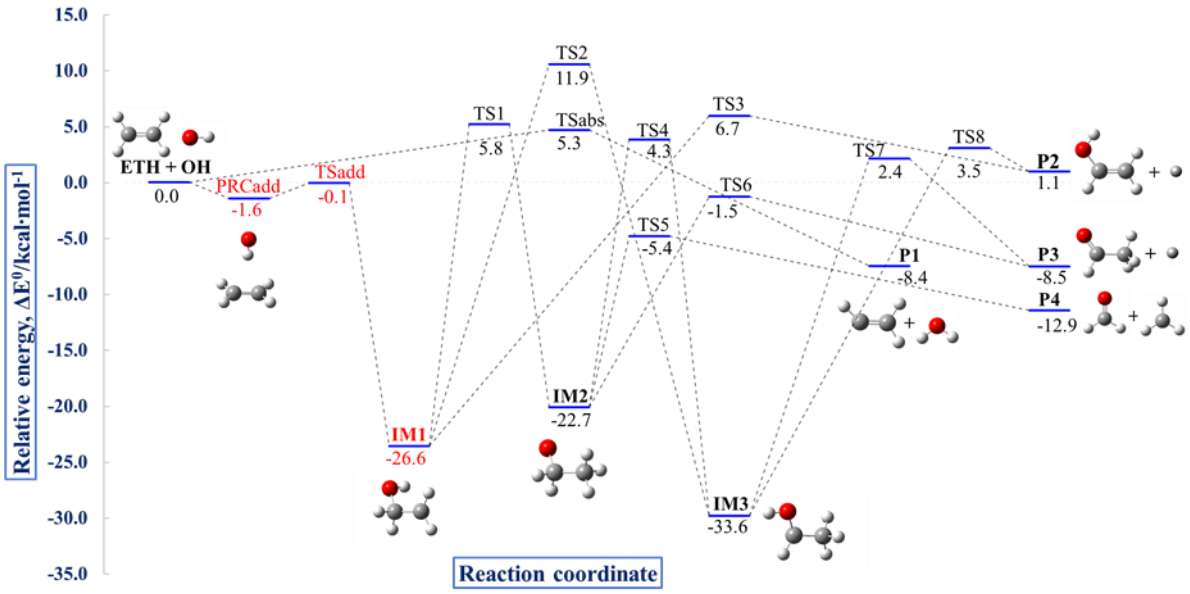

Figure 1. Potential energy surface for the CH_2=CH_2 + OH reaction obtained at the jChS//rev-DSD-PBEP86-D3(BJ)/jun-cc-pV(T+*d*)Z level of theory. Relative energies include ZPVEs. Cartesian coordinates and figures of all the stationary points are reported in the Supporting Information.

3.1.2. Global rate constant

The global rate constants in the high-pressure limit computed for the CH_2=CH_2 + OH reaction as a function of temperature over the 100-600 K range are presented in Figure 2, where they are compared with experimental measurements. [64–66] In this respect, it has to be noted that experiments often fall short of reaching sufficiently high pressures to directly measure the high-pressure limit. However, three investigations[64–66] attempted to extract the high-pressure limit by fitting the pressure dependence with the help of theoretical guidance. Theoretical results obtained with a similar approach to that applied in the current study, [48] are also included in Figure 2.

The rate constants obtained in the present work agree very well with the available experimental data, both for the values (within a factor of 1.5) and, notably, the temperature dependence. The current findings also align closely with the theoretical predictions of Greenwald et al. [48] with relatively small deviations at low and high temperatures. At temperatures below 200 K, our results show an unprecedented agreement with the only available experimental data set worked out by Vakhtin and co-workers, [65] while moving to atmospherically relevant temperatures, there is an excellent agreement with the determinations by Cleary et al.[6472] Above 400 K experiments were mostly performed at ambient pressure. In

fact, only Fulle et al. [66] reported rate constants for the high-pressure limit, that were however extrapolated and not directly measured, resulting in a 19% discrepancy with the presently computed data. By a closer inspection of Figure 2, a clear shift from negative to positive temperature dependence can be observed around 450 K. From a theoretical point of view, this change can be attributed to the passing from a competition between the outer and inner transition states, to a complete dominance of the inner transition state. This transition can be rationalized in terms of the increasing population of high-energy states with the rise in temperature, that will surpass the reactant asymptote at the inner transition state. Consequently, this transition state behaves as a non-submerged barrier, resulting in a positive activation energy and a positive temperature dependence.

The calculated global rate constant is found to be pressure-dependent under the considered conditions, a result that agrees with previous experimental and theoretical studies, [48,64,65,67,68,70] as illustrated in Figure 3. The fitting of our theoretical results to the pressure dependence of the experimental data provided us with the downward energy transfer parameter value of $\langle \Delta E_{down} \rangle = 260(T/300)^{0.9}$ cm^{-1}. This updated value aligns closely to those commonly observed in collisions involving a N_2 bath gas and it is found in line with other recent fittings in the literature.[74]

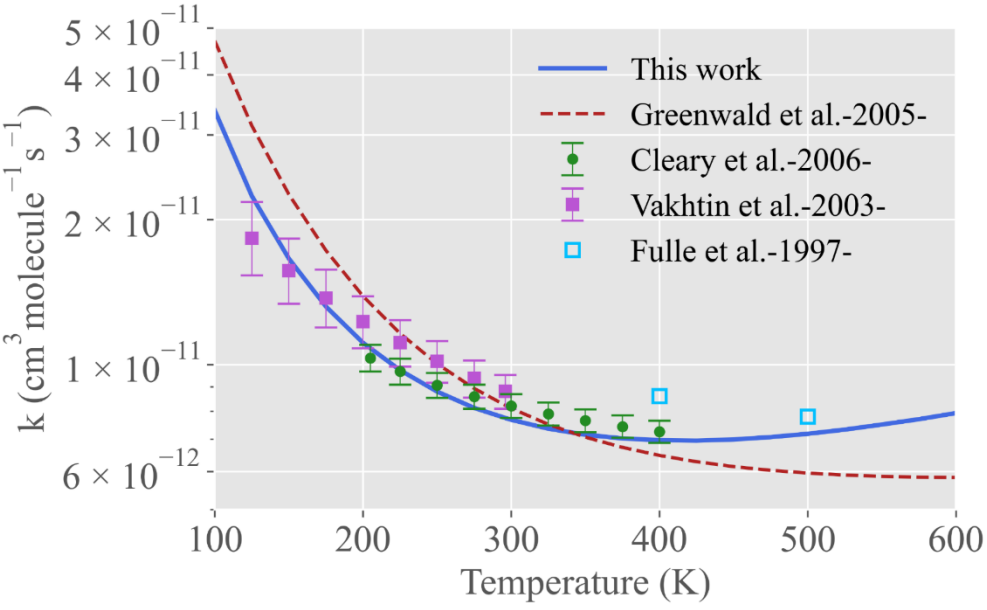

Figure 2. High-pressure limit global rate constants as a function of temperature for the CH_2=CH_2 + OH reaction. Also reported are the experimental data from Cleary et al. [64], Vakhtin et al. [65], Fulle et al. [66], and theoretical data from Greenwald et al. [48]

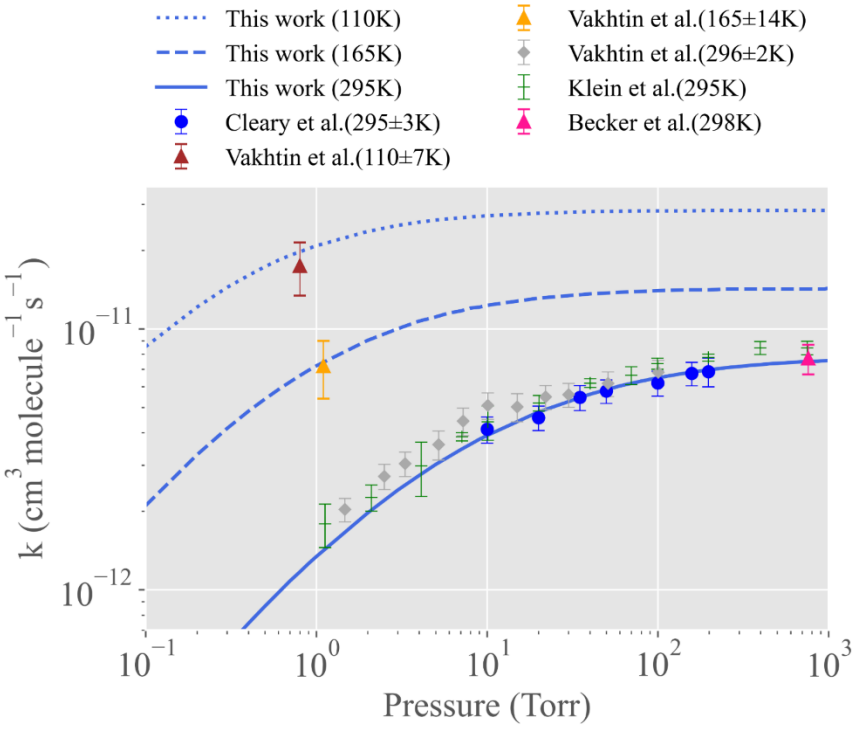

Figure 3. Plot of the predicted pressure dependence of the global rate coefficient for the CH_2=CH_2 + OH reaction at different temperatures. Also plotted are the corresponding experimentally observed rate coefficients with N_2 as bath gas.

3.1.3. Product distributions

The phenomenological rate coefficients of the first addition intermediate, H-abstraction, and the main bimolecular product exit channels for the reaction between CH_2=CH_2 and OH at atmospheric pressure are shown in Figure 4. At ambient pressure, stabilization of the 2-hydroxyethyl radical (IM1: CH_2CH_2OH) adduct is the dominant pathway over the whole temperature range studied. When increasing the temperature, the H-abstraction process starts becoming important, but still far from competing with the addition. Master equation simulations performed in the theoretical work by Senosian et al.[70] showed that under all the investigated conditions, the isomerization reactions to IM2 and IM3 are too slow and, therefore, do not compete with the main addition reaction, clearly demonstrating that the CH_2=CH_2 + OH reaction produces mainly IM1, which is then stabilized by third-body collisions. A closer look at Figure 4 reveals a noticeable shift in the production of P1 (CH_2CH + H_2O) and P4 (CH_3 + CH_2O) around 220 K, a phenomenon that has not been previously documented in the literature.

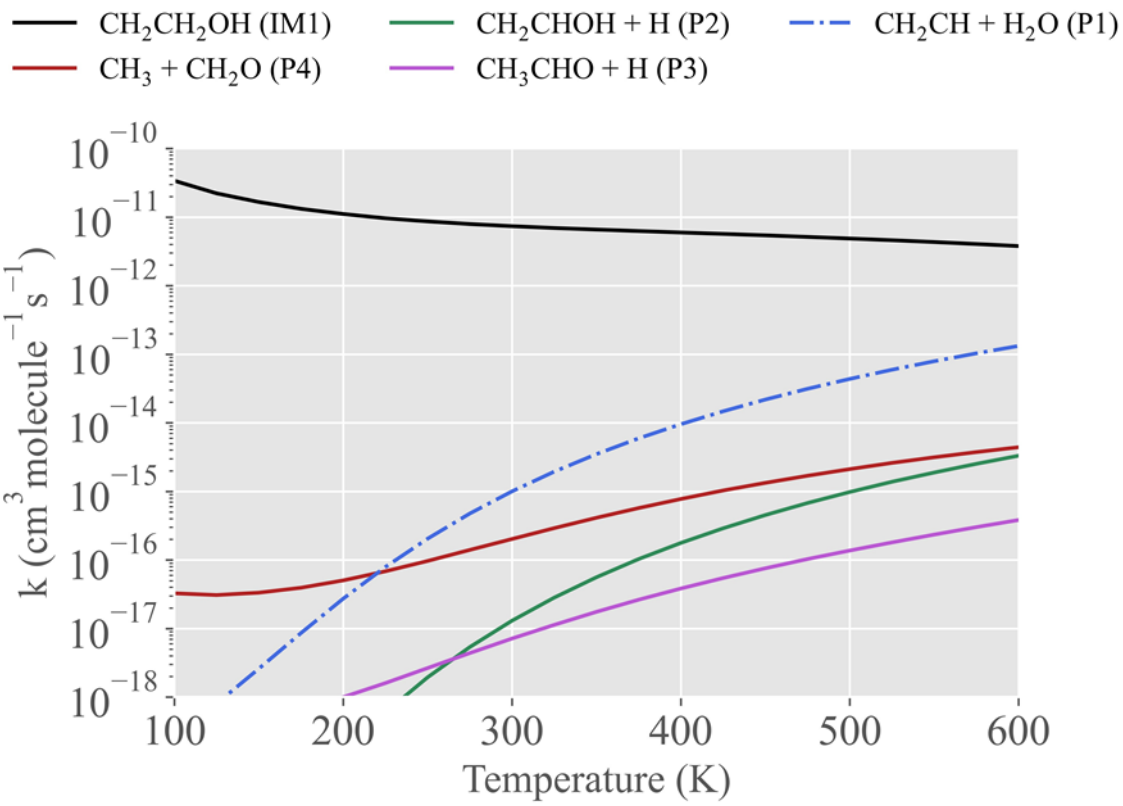

Figure 4. Product distributions for the CH_2=CH_2 + OH reaction at 1 atm over the 100 – 600 K temperature range.

The excellent agreement of the predicted rate constants and their temperature and pressure dependence obtained for CH_2=CH_2 with the available experimental results demonstrates the reliability of the thermochemical and kinetic predictions of the present computational protocol, which therefore can be safely adopted to investigate the OH-initiated degradation of CF_2=CHF and CCl_2=CHCl.

3.2. CF_2=CHF + OH

3.2.1. Thermodynamic evaluation

The potential energy surface ruling the addition of OH to the – CF_2 moiety is shown in Fig. 5 (a), while the H-abstraction and addition to the – CHF moiety are shown in Fig. 5 (b). For both abstraction and addition pathways, weakly bound pre-reactive complexes PRCabs and PRCadd were identified, in all cases with energies about 1.6 kcal mol^{-1} below the reactants. The main products from the H-abstraction channel are water and the trifluoro-vinyl radical (P4: C_2F_3

+ H_2O), after surpassing a relatively high energy barrier (TSabs) of 9.7 kcal mol^{-1}. Concerning the OH addition to the double bond, two very stable species, the hydroxyl-fluoroalkyl intermediate radicals IM1 and IM4, can form from the pre-reactive complex PRCadd by overcoming the corresponding submerged transition states $TSadd_{CF2}$ (-1.5 kcal mol^{-1}) and $TSadd_{CHF}$ (-0.9 kcal mol^{-1}), respectively. The subsequent reaction paths that emerge from different unimolecular isomerization and dissociation reactions of IM1 and IM4 are analyzed in the following.

IM1 ($CHFCF_2OH$) has three possible reaction pathways, as can be seen in Fig. 5 (a). (*i*) Intramolecular F-atom transfer via transition state TS1 (-10.9 kcal mol^{-1}) from the carbon radical site to the adjacent carbon, forming CHF_2CFOH (IM2, -46 kcal mol^{-1}) which can lead to the fluoroacetyl fluoride radical (P3: CHFCFO + HF) through HF elimination (TS4, -15.9 kcal mol^{-1}). (*ii*) Isomerization to (a) CH_2FCF_2O (IM3, -36.3 kcal mol^{-1}) via [1,3] hydrogen shift (TS2, -14.4 kcal mol^{-1}) which yields fluoroacetyl fluoride and F atoms (P1: CH_2FCFO+F) after overcoming TS6 (-7.6 kcal mol^{-1}). Alternatively, IM1 can lead to (*b*) difluoroketone and the fluoromethyl radical (P2: CH_2F+CF_2O) through F-atom and carbon-carbon β-scission involving TS5 (-30.6 kcal mol^{-1}). (*iii*) Formation of fluoroacetyl fluoride radical (P3: CHFCFO + HF) after passing a barrier of 33.5 kcal mol^{-1} (TS3).

The intermediate IM4 (CF_2CHFOH) has also three transformation pathways detailed in Fig. 5 (b). (*i*) Similarly to IM1, it can undergo an intramolecular F-atom shift (TS7, -11.9 kcal mol^{-1}) to generate CF_3CHOH (IM5, -56.2 kcal mol^{-1}) which then decomposes to fluoral and H atom (P6: CF_3CHO + H) or to the CF_2CHO radical and hydrogen fluoride (P5: CF_2CHO + HF), after overcoming the submerged transition TS10 (-11.8 kcal mol^{-1}) and TS11 (-19.6 kcal mol^{-1}), respectively. IM5 can also isomerize to CF_3CH_2O (IM7, -39.4 kcal mol^{-1}) though the submerged transition state TS14 (-14.2 kcal mol^{-1}) which subsequently undergoes β-scission of the C–C bond (TS15, -21.6 kcal mol^{-1}) leading to formaldehyde and the trifluoromethyl radical (P9: CH_2O+CF_3). (*ii*) Intramolecular H-atom transfer from the OH-group via the four-membered ring transition state TS8 (-3.1 kcal mol^{-1}) can lead to the formation of the alkoxy radical CF_2HCHFO (IM6, -37.7 kcal mol^{-1}) that in turn can evolve to produce either difluoroacetyl fluoride and H atoms (P7: CF_2HCFO + H) or formyl fluoride and difluoromethyl radical (P8: CF_2H+CHFO) by H-atom elimination (TS13, -18.3 kcal mol^{-1}) and β-cleavage of the C–C bond (TS12, -30.3 kcal mol^{-1}), respectively. (*iii*) HF-elimination proceeding through TS9 (-8.3 kcal mol^{-1}) can also lead to the difluoroacetaldehyde radical (P5: CF_2CHO + HF).

The present results can be compared with those reported by Snitsiriwat et al.[17] performed at the M06-2X and CBS-QB3 levels of theory. While a fair agreement is observed for a part of the reactive PES (highlighted in red in Figure 5), H- and F-elimination pathways ruled by TSs lying too much above the reactants have not been included in our PES. Instead, additional OH-degradation first generation products of atmospheric relevance like formaldehyde and trifluoromethyl radical (P9) which were not reported previously, have been identified as both thermodynamically and kinetically viable exit channels.

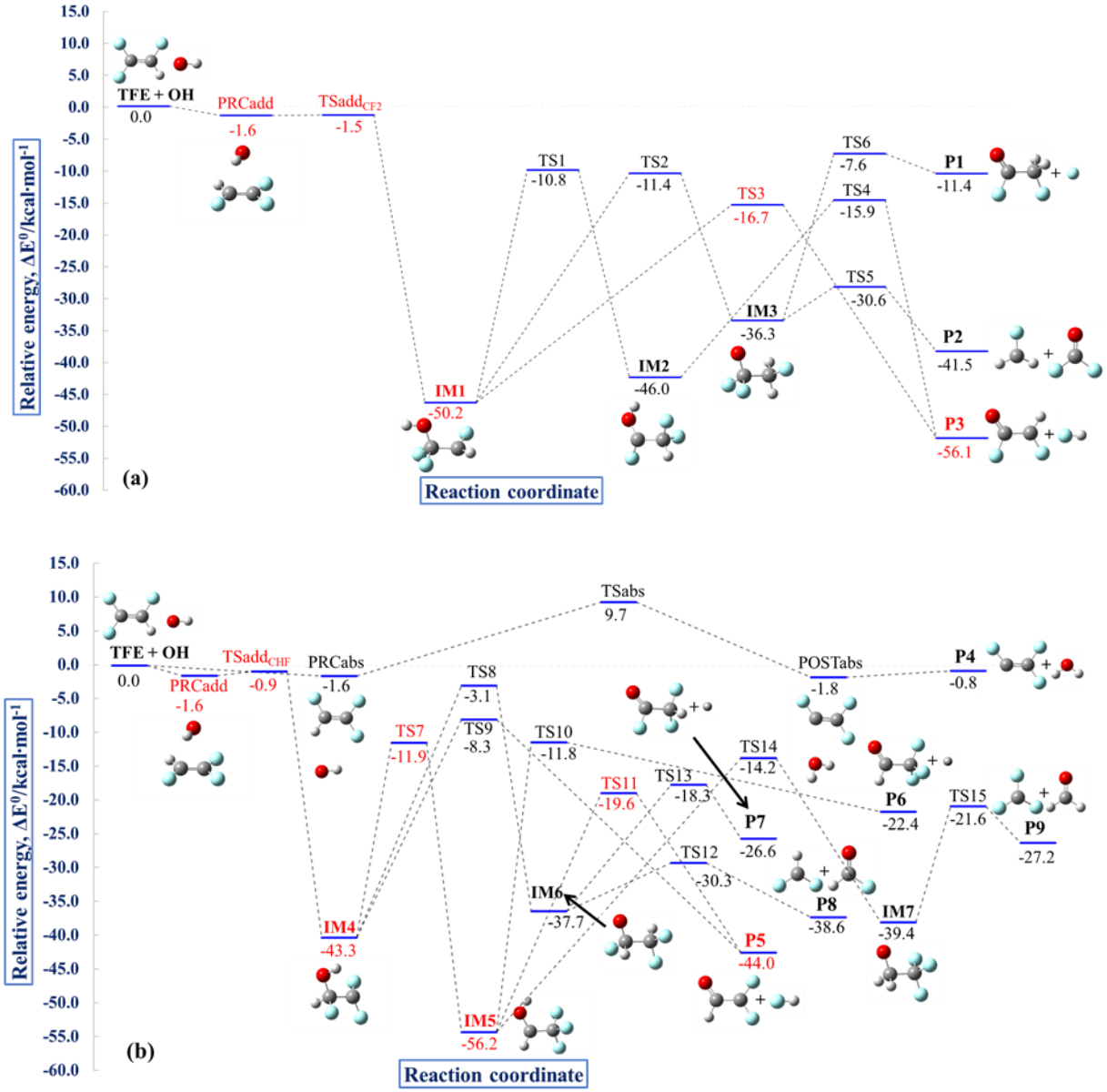

Figure 5. Potential energy surfaces for the CF_2=CHF + OH reaction obtained at jChS//rev-DSD-PBEP86/jun-cc-pV(T+*d*)Z-D3(BJ) level of theory. (a) OH addition to the – CF_2 fragment; (b) H-abstraction from and OH addition to the – CHF fragment. Cartesian coordinates and figures of all the stationary points are reported in the Supporting Information.

3.2.2 Global rate constant

The global rate constants obtained for the reaction between CF_2=CHF and the OH radical based on the reactive PES described in the previous subsection are shown in Figure 6, along with the limited available experimental data. [14–16] It is apparent that our results are in excellent agreement with their experimental counterparts (maximum discrepancy of a factor of 1.3), and, in particular, both theory and experiments[15,16] agree in forecasting an almost pressure-independent global rate constant under the considered conditions. The rate constants in the high pressure limit recently worked out by using conventional transition state theory on top of a PES evaluated at M06-2X and CBS-QB3 levels of theory are in good agreement with the experimental outcome at room temperature. [17] However, by decreasing the temperature, the rate constant calculated from the Arrhenius expression given in Ref.17 (3.27×10^{-11} cm^3 $molecule^{-1}$ s^{-1} at 200 K) is almost 3 times larger than the value calculated from the Arrhenius parameters recently derived experimentally[16] (1.2×10^{-11} cm^3 $molecule^{-1}$ s^{-1} at 200 K) as well as to that predicted in the present work (1.14×10^{-11} cm^3 $molecule^{-1}$ s^{-1}).. This discrepancy is most probably caused by the kinetic model utilized in Ref.17, which ignores the dynamics in the outer transition state region that, as previously demonstrated by Greenwald and co-workers, [48] represents the dominant dynamical bottleneck at low temperatures.

Another interesting detail that can be seen observing Figure 6 is that the theoretical predictions show an upward trend above 450 K, contrary to the negative temperature dependence provided by experiments performed between 250 – 430 K. As previously analysed for the CH_2=CH_2 + OH reaction, this trend reversal is due to the dominance of the inner transition state at high temperatures.

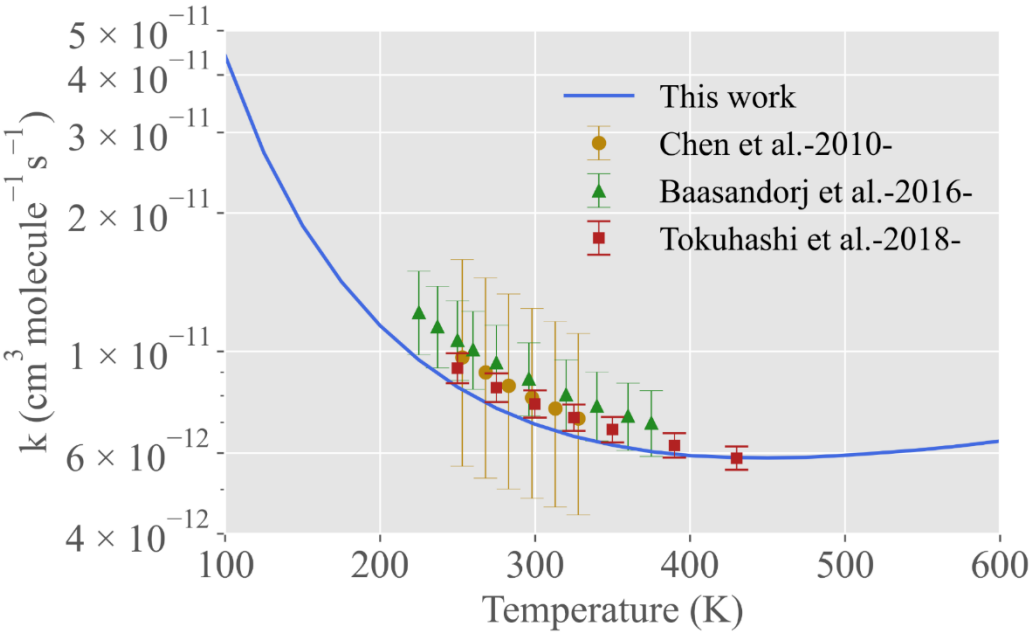

Figure 6. Global rate constant as a function of temperature for the CF_2=CHF + OH reaction. Also reported are the available experimental data from Chen et al.[13], Baasandorj et al.[14] and Tokuhashi et al.[15]

3.2.2. Product distributions

The product distributions for the CF_2=CHF + OH reaction at P = 1 atm are shown in Figure 7. Below 350 K, the electrophilic π-addition to the – CF_2 group is favored over that to the – CHF site, whereas just the opposite occurs above 400 K, even if the addition on the – CF_2 site is governed by an energy barrier lower than that ruling the addition to the – CHF moiety (see Fig. 5). Since this behavior is observed also in the high-pressure limit, it can be speculated that it is caused by a transition from enthalpic to entropic control, with the role of the latter contribution to the Gibbs free energy increasing as the temperature raises. In contrast to the previous study by Snitsiriwat et al., [17] we found that the dominant reaction channels at temperatures above 450 K are the HF molecular eliminations from $CHFCF_2OH$ (IM1) and CF_2CHFOH (IM4), forming CHFCFO (P3) and CF_2CHO (P5). The third important pathway at temperatures below 300 K is the formation of CH_2F + CF_2O (P2) via β-scission from CH_2FCF_2O (IM3). With increasing temperature, the formation of CF_3CHO + H (P6) and CF_3 + CH_2O (P9) starts to overtake the formation of P2, ending up as the second major product at temperatures above 350 K. The formation of CF_2HCFO + H (P7) by H elimination from the CF_2HCHFO (IM6) adduct is not significant compared to all other pathways at the temperatures studied.

In agreement with previous studies, [75–78] the results of the more refined kinetic model employed in the present study for the H-abstraction process (variational treatment, multidimensional tunneling, anharmonicity) confirm that the role of the H-abstraction reaction is negligible for fluorinated olefins under atmospheric conditions. Furthermore, the high strength of the C-F bond leads to a negligible role of the F-atom elimination over the whole temperature range.

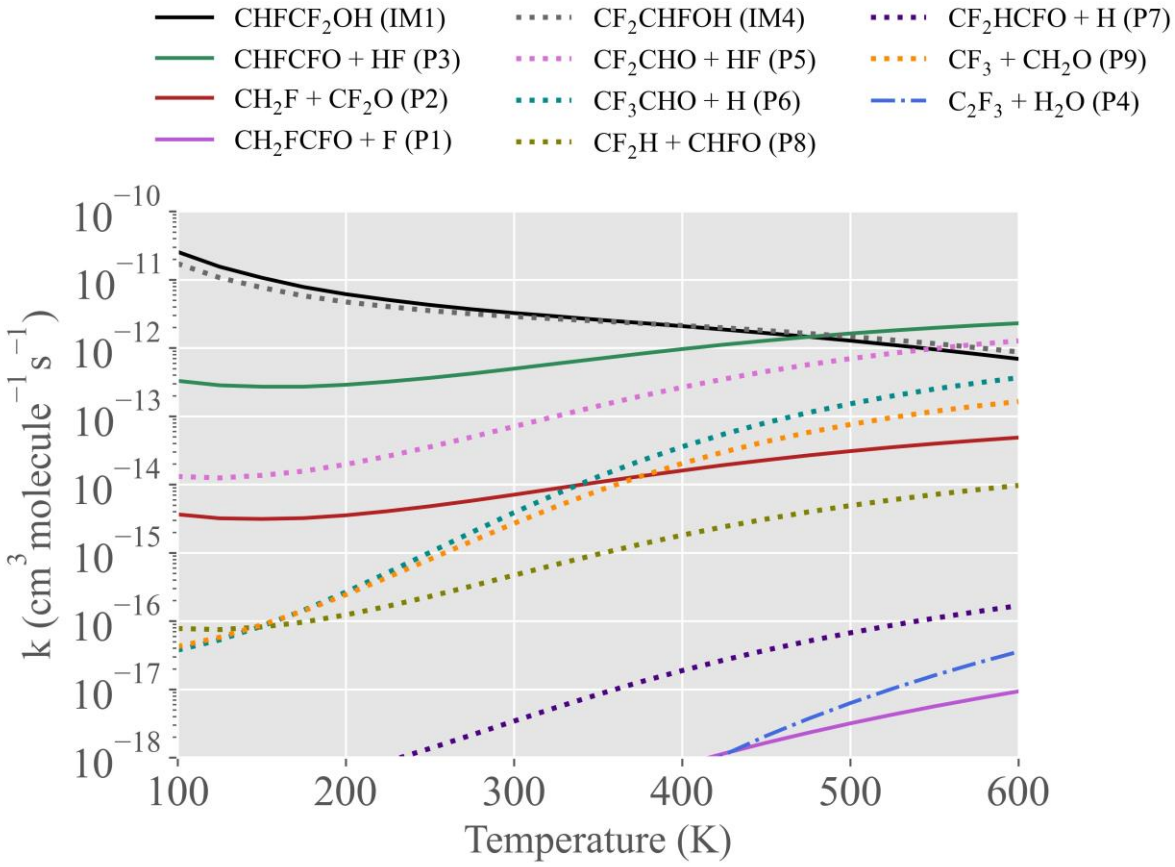

Figure 7. Product distributions for the CF_2=CHF + OH reaction at 1 atm over the 100 – 600 K temperature range.

3.3. CCl_2=CHCl + OH

3.3.1. Thermodynamic evaluation

Both addition and abstraction mechanisms have been considered for the CCl_2=CHCl + OH reaction: the PES for the H-abstraction and OH addition to the – CHCl fragment are shown in Fig. 8 (a), whereas the PES for the OH addition to the – CCl_2 fragment is shown in Figure 8 (b). In contrast to CH_2=CH_2 and CF_2=CHF, the H-abstraction pathway that produces the

trichloro-vinyl radical and water (P1: $C_2Cl_3 + H_2O$) appears unlikely to occur under atmospheric conditions, as it involves a very high energy barrier of 31.6 kcal mol^{-1} (TSabs in Figure 8 (a)). The addition reaction starts with the formation of the weakly-bound pre-reactive complex PRCadd that lies 1.7 kcal mol^{-1} below the reactants. The two generated hydroxyl chloroalkyl adduct radicals IM1 ($CCl_2CHClOH$) and IM4 ($CHClCCl_2OH$) undergo subsequent unimolecular isomerization and dissociation reactions, after PRCadd overcomes the transition states, $TSadd_{CHCl}$ (-0.4 kcal mol^{-1}) and $TSadd_{CCl2}$ (2.2 kcal mol^{-1}), respectively. IM1 has four possible reaction pathways, as it can be seen in Fig. 8 (a). (*i*) It can form dichloro vinyl alcohol (P3: CCl_2CHOH + Cl) via barrierless Cl-elimination. (*ii*) Through transition state TS1 (-24.5 kcal mol^{-1}), the IM1 adduct can undergo isomerization leading to the formation of CCl_3CHOH (IM2) which can then dissociate to produce dichloro-vinyl alcohol (P3) via a barrierless pathway. (*iii*) Isomerization through [1,3] hydrogen shift (TS2, 5.0 kcal mol^{-1}) leads to $CCl_2HCHClO$ (IM3) which can evolve further to a range of products. Those include chloroketone and the dichloro-methyl radical (P4), trichloro-acetyl chloride and H atoms (P5), dichloro-oxirane and Cl atoms (P6) and dichloro-acetaldehyde and Cl atoms (P7), which involve the transition states TS4 (-15.7 kcal mol^{-1}), TS5 (-2.7 kcal mol^{-1}), TS6 (12.1 kcal mol^{-1}), and TS7 (19.1 kcal mol^{-1}), respectively. (*iv*) H-elimination via TS3 (8.9 kcal mol^{-1}) yields trichloro-ethanol (P2), the least thermodynamically favored product.

IM4 ($CCl_2CHClOH$) has three possible exit channels in Fig. 8 (b). (*i*) Similarly to IM1, a barrierless Cl-elimination results in the formation of dichloro-vinyl alcohol (P12). (*ii*) Isomerization via the submerged TS8 (-25.9 kcal mol^{-1}) leads to $CHCl_2CClOH$ (IM5, -37.4 kcal mol^{-1}), which in turn can dissociate via a barrierless pathway to produce P12 or undergo HCl elimination through TS11 (5.7 kcal mol^{-1}) to form dichloro-acetaldehyde radical (P9). (*iii*) [1,3] hydrogen shift via the transition state TS9 (2.3 kcal mol^{-1}) yields the $CH_2ClCCl_2(O)$ radical (IM6, -22.8 kcal mol^{-1}), from which various products can form, including dichloro-ketone and the chloromethyl radical (P8), dichloro-oxirane and Cl atoms (P11) and chloro-acetyl chloride and Cl atoms (P10). These reactions involve transition states TS10 (-17.9 kcal mol^{-1}), TS13 (7.1 kcal mol^{-1}), and TS12 (17.8 kcal mol^{-1}), respectively.

To the best of our knowledge there are only two previous theoretical investigations dealing with the mechanism of the reaction between CCl_2=CHCl and OH, [10,11] which is a potential source of Cl atoms in the atmosphere. The main conclusion of the study performed by Tichenor and co-workers was that at room temperature the dominant reaction channel is the adduct stabilization, [11] while Cl-elimination occurs at much higher temperatures (1000 K). The second

study, performed by Christiansen and Francisco,[10] presented a general atmospheric oxidation scheme for this reaction. The influence of the Cl atom on the whole oxidation reaction was studied analyzing also the influence of the generation of Cl atoms during the CCl_2=CHCl + OH reaction on the overall chemical kinetics. However, none of the afore mentioned references provided a comprehensive study of the mechanistic and kinetic details for this specific reaction.

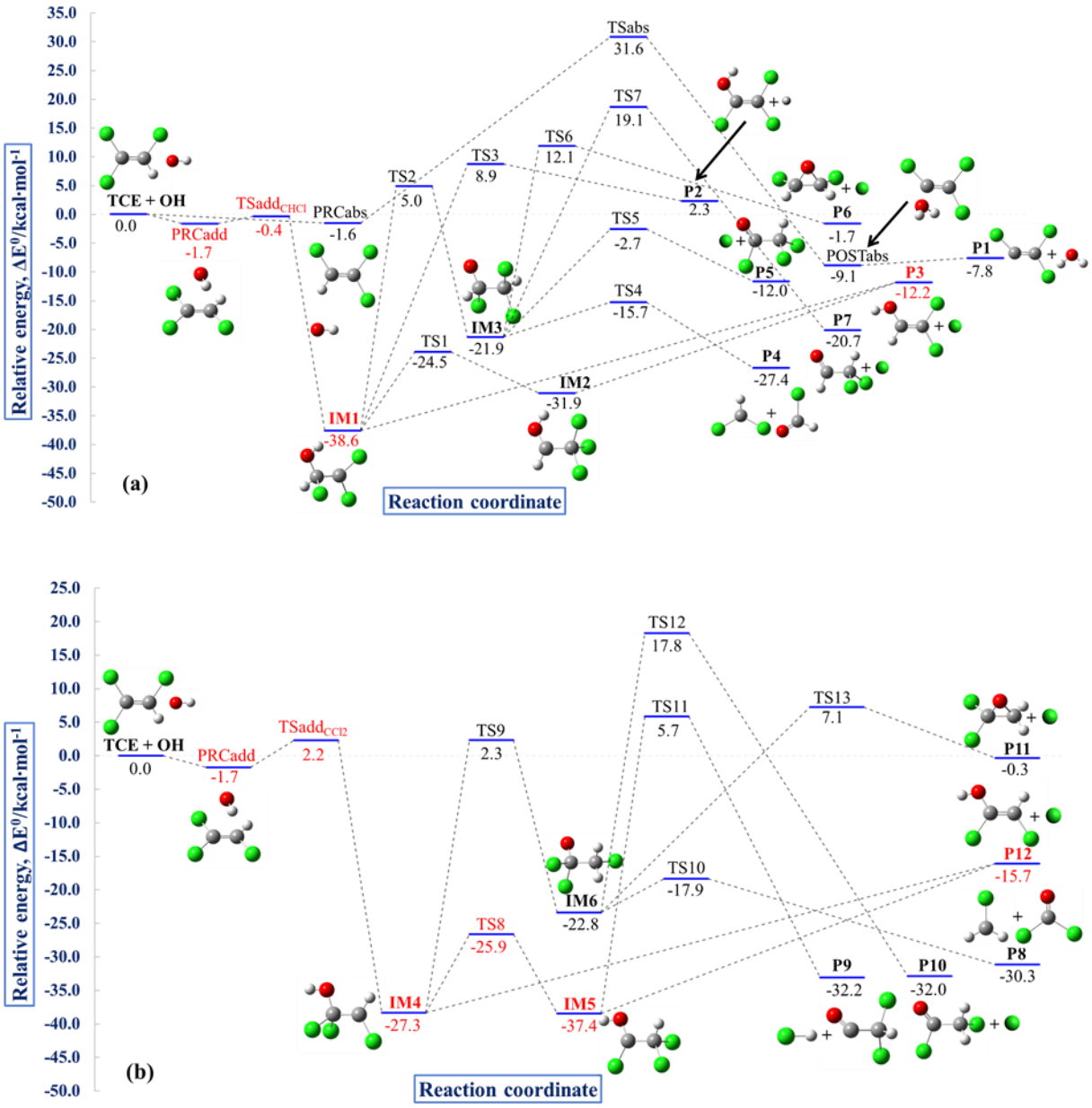

Figure 8. Potential energy surfaces for the OH + CCl_2=CHCl reaction obtained at jChS//rev-DSD-PBEP86-D3(BJ)/jun-cc-pV(T+*d*)Z level. (a) H-abstraction and OH-addition to the – CHCl fragment; (b) OH-addition to the – CCl2 fragment. Cartesian coordinates and figures of all the stationary points are reported in the Supporting Information.

3.3.2. Global rate constant

Our estimate of the global rate constant for the CCl_2=CHCl + OH reaction is found to be 2.28×10^{-12} cm^3 $molecule^{-1}$ s^{-1}, in excellent agreement with previous theoretical and experimental studies[11,79–83] and the recommended values by Atkinson et al.[84]. Higher temperature predictions show the same behavior as the measurements by Tichenor et al., [11] but lie about 40% higher in magnitude. As can be seen in Figure 9, in comparison with ETH and TFE, the temperature dependence switches from negative to positive at lower temperatures (300 K). The complexity in this trend could be theoretically attributed to the non-submerged inner transition state for addition to the $–CCl_2$ moiety, contrary to the submerged addition to the –CHCl moiety, demonstrating that the kinetics are dominated by the inner transition states even at relatively low temperatures. This, however, cannot fully explain the slight discrepancy between experimental measurements and our theoretical predictions. Given the significant role of chlorine atoms in TCE's atmospheric degradation and the fact that Cl elimination reactions are found to be dominant across all temperatures studied (as will be shown in the following paragraph), further kinetic studies on secondary Cl-reactivity should be encouraged in order to acquire more insight for this complicated system. The theoretical investigation on the mechanism and kinetics of the Cl-initiated oxidation of TCE is presently under way in our group and will be reported in a future study.

In analogy to CF_2=CHF, master equation simulations do not show any pressure dependence of the overall rate constant over the temperature range studied, with this feature being again consistent with the experimental studies. [11,82]

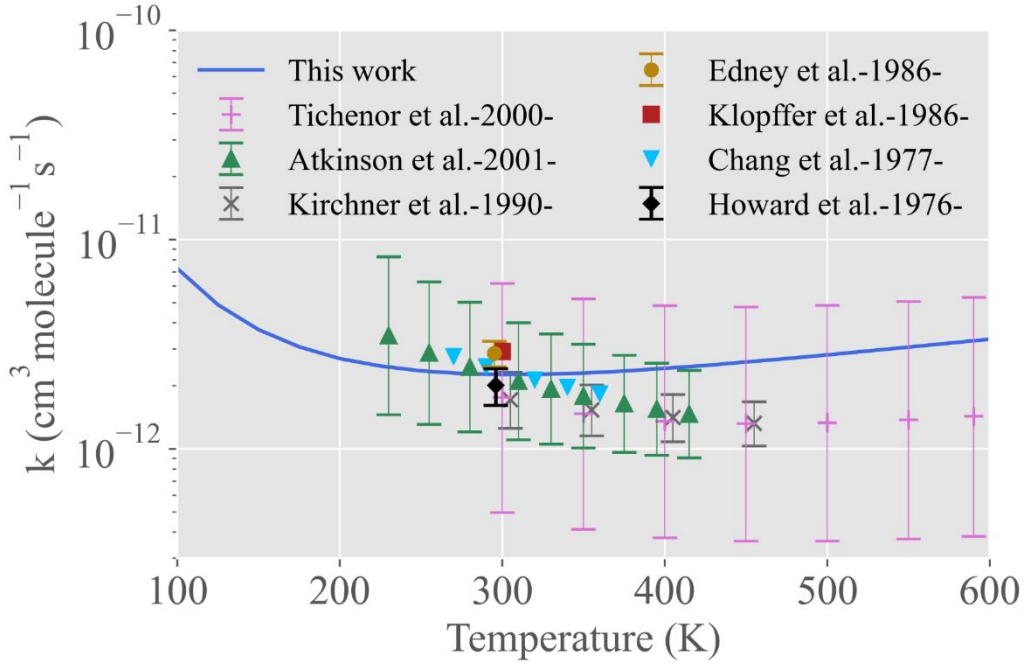

Figure 9. Global rate constant as a function of temperature for the CCl_2=CHCl + OH reaction. Also reported are the available experimental data from Tichenor et al. [11], Kirchner et al. [79], Edney et al. [80], Klopffer et al. [81], Chang et al[82], Howard et al. [83], and recommended values by Atkinson et al. [84]

3.3.3. Product distributions

The product distributions for the CCl_2=CHCl + OH reaction at P = 1 atm are shown in Figure 10. It is apparent that the Cl elimination reaction, which produces CCl_2CHOH (P3), is the main channel over the whole temperature range. The stabilization reaction leading to the addition adduct CCl_2CHClOH (IM1) is the second important reaction channel at low temperatures, but around 200 K, Cl elimination yielding CHClCClOH + Cl (P12) starts to take over and remains dominant up to 600 K. At higher temperatures, other key processes include either removal of HCl from IM5 to generate $CHCl_2$CO (P9) or formation of CHClO + $CHCl_2$ (P4) and CCl_2O + CH_2Cl (P8) through β-scission reactions. Elimination of H atoms involves high barriers hence they proceed slowly giving small yields. In analogy to TFE, the H-abstraction reaction is negligible and does not rival the addition and subsequent isomerization routes under atmospheric conditions. Experimental studies provided contradictory results concerning product yields. Nolan et al.[8] proposed that the HCl elimination pathways should be the dominant channels, whereas Tuazon et al.[9] argued that the OH-initiated oxidation of CCl_2=CHCl results in the formation of chlorine atoms which, in turn, trigger the Cl-initiated degradation of CCl_2=CHCl. This process was theoretically examined by Francisco and co-

workers,[10] who demonstrated that the key mechanisms include the formation of chlorine atoms that will further oxidize CCl_2=CHCl, changing in this way substantially the product yields.

The results here obtained further support these latter findings [9,10] showing that the principal routes of the OH-initiated oxidation of CCl_2=CHCl under atmospheric conditions lead to the production of chlorine atoms. In passing, it should be noted that the Quantum Rice-Ramsperger-Kassel (QRRK) modeling performed by Tichenor et al.[86] suggested that the adduct stabilization reaction accounts for 85% of the overall reaction at 1 atm and 298 K. This result is in disagreement with our findings and with the experimental results, which showed that Cl elimination is the primary reaction path. This provides a further proof that accurate computational protocols for thermochemistry and state-of-the-art kinetic models such as VRC-VTST combined with ME simulations, are crucial to reliably simulate overall rate constants, as well as the branching ratios and product yields.

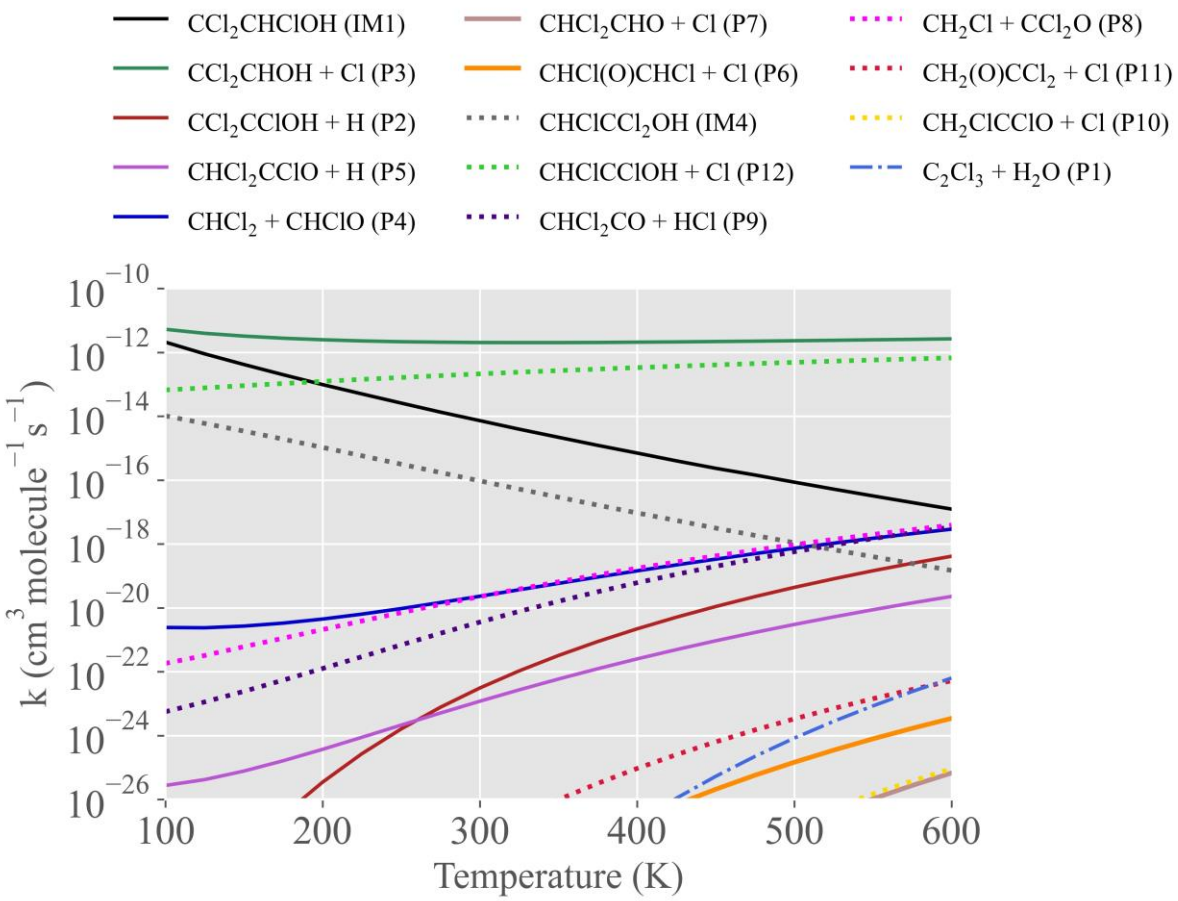

Figure 10. Product distributions for the CCl_2=CHCl + OH reaction at 1 atm over the 100 – 600 K temperature range.

3.4. General remarks and comparisons

The global rate constants for the CH_2=CH_2 + OH, CF_2=CHF + OH and CCl_2=CHCl + OH reactions at P = 1 atm and in the high-pressure limit are listed in Table 2. A first observation is that the ETH's reactivity is influenced by the pressure, whereas those of TFE and TCE remain almost unaffected under atmospheric temperatures. The replacement of hydrogen by fluorine does not considerably alter the reactivity with the OH radical, whereas the substitution with chlorine reduces the reactivity of olefins towards the OH radical by a factor of ~3. This could be due to the inductive effect of the Cl atom, which reduces the electron density of the C=C bond and deactivates the electrophilic attack of the OH radical.

Table 2. Calculated total rate constants (in units of 10^{-12} cm^3 $molecule^{-1}$ s^{-1}) for the three reactions, $CH_2=CH_2$ + OH, $CF_2=CHF$ + OH and $CCl_2=CHCl$ + OH, at P = 1 atm and P = ∞ atm.

Temperature (K)	*$CH_2=CH_2$ + OH*		*$CF_2=CHF$ + OH*		*$CCl_2=CHCl$ + OH*	
	∞ atm	1 atm	∞ atm	1 atm	∞ atm	1 atm
100	33.7	33.7	44.1	43.1	7.26	7.26
150	16.6	16.6	18.8	18.8	3.71	3.71
200	11.1	11.1	11.4	11.2	2.70	2.70
250	8.79	8.66	8.35	8.31	2.36	2.36
300	7.68	7.37	6.93	6.90	2.26	2.26
350	7.15	6.58	6.24	6.22	2.30	2.30
400	6.96	5.96	5.92	5.91	2.42	2.42
450	6.97	5.42	5.85	5.83	2.60	2.60
500	7.14	4.87	5.93	5.88	2.81	2.81
550	7.43	4.33	6.10	6.03	3.06	3.06
600	7.80	3.79	6.37	6.24	3.34	3.34

Another noteworthy observation is that in the limit of infinite pressure and low temperatures (T=100 K), the reactivity of $CF_2=CHF$ is higher than that of ethylene. However, when the temperature reaches 200 K, ETH becomes more reactive than its fluorinated counterpart. This implies that long-range interactions, which govern the dynamics at low temperatures, are more important in the case of fluorinated olefins.

The dominant influence of steric parameters on the regioselectivity of free radical addition has been pointed out long time ago by many groups and different textbooks, that have explained the favored addition in terms of the different stability of the newly formed radical centers. [85,86] This rule applies also here in the case of TCE, where IM1 ($CCl_2CHClOH$) that comes from the addition to the – CHCl part is the more stable one, while in the case of TFE the more stable IM1 ($CHFCF_2OH$) emerges from the addition to the – CF_2 fragment. In order to better understand the OH-addition reactivity patterns of the two halogenated olefins, we performed Natural Bond Analysis (NBO)[87] calculations for all 4 transition states involved and determined the different charge distribution appointed to both fragments, – CX_2 or – CHX (X=F, Cl). As obvious from Figure 11, the OH radical will prefer to attack the most electrophilic C atom in the – CF_2 fragment (total charge 0.173) than the– CHF (0.046). The opposite occurs for $CCl_2=CHCl$ where – CCl_2 accumulates a total charge of 0.074 and the preferred – CHCl part 0.950.

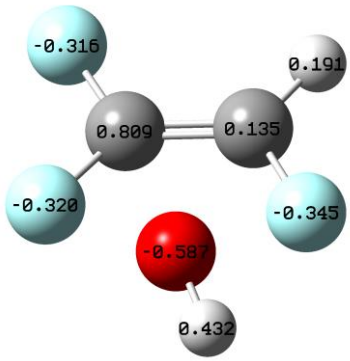

TSadd$_{CF2}$

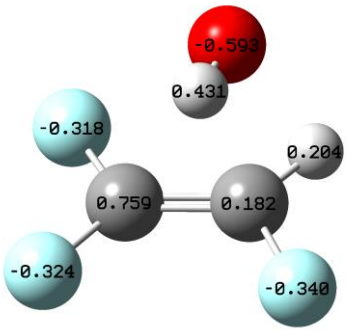

TSadd$_{CHF}$

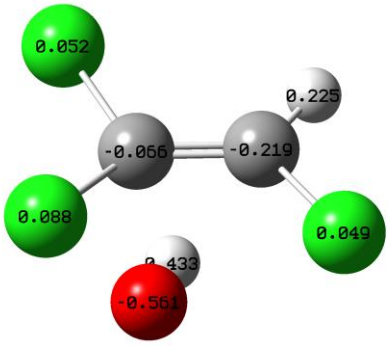

TSadd$_{CCl2}$

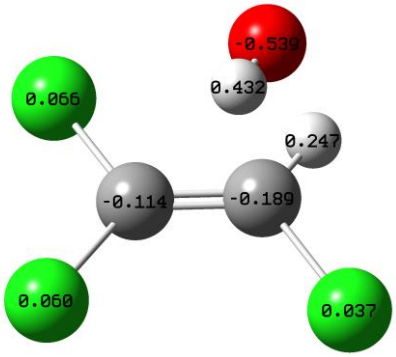

TSadd$_{CHCl}$

Figure 11. Natural Bond Orbital charges for the four transition states involved in the OH addition to CX_2=CHX (X = F, Cl) at the rev-DSDPBEP86-D3(BJ)/jun-cc-pV(T+*d*)Z level of theory.

3.5. Atmospheric implications

A detailed knowledge of the overall rate constants for the OH-initiated degradation of atmospheric pollutants is of significant atmospheric relevance since it allows the evaluation of the lifetimes of important intermediates, that are associated to the most important sink processes. As a matter of fact, variations in the OH radical's column density over different atmospheric conditions (temperature, pressure)[88] and various transport mechanisms, have been found to contribute to a significant change in the loss rate of a chemical substance. As a consequence, the definition of a single atmospheric lifetime for very short-lived species, like the olefins considered here, is far from simple and, for certain aspects, conceptually questionable because these molecules are not well mixed in the atmosphere and their temporal distribution depends on the conditions at the emission point.[5]

The rate constants here computed for the reactions between CX_2=CHX (X = H, F, and Cl) have been used to provide the atmospheric lifetimes (τ) of ethylene, trifluoroethylene and trichloroethylene along different altitudes in the atmosphere (h), as a function of pressure (P),

temperature (T) and [OH] concentration, all collected in Table 3. For this purpose, the relative method proposed by Prather and Spivakovsky[89] has been adopted, which makes use of a reference compound whose global budget and atmospheric lifetime are well characterized, to scale the rate coefficients for the reaction of the target species against the OH radical:

$$\tau_{\mathrm{X}} = \frac{k(\mathrm{REF+OH})}{k(\mathrm{X+OH})}\tau_{\mathrm{REF}} \qquad (1)$$

where τ_{X} is the lifetime of the target species, $k(\mathrm{X+OH})$ and $k(\mathrm{REF+OH})$ are respectively the rate constants for the reaction between the OH radical and the target and the reference compounds, and τ_{REF} is the lifetime for the latter. Methyl-chloroform, with an atmospheric lifetime of 6.1 years, has been used as reference compound and the corresponding temperature dependent rate constants have been taken from ref. [90]

Table 3. Altitude dependent atmospheric lifetimes of CH_2=CH_2 (*ETH*), CF_2=CHF (*TFE*) and CCl_2=CHCl (*TCE*).

H (km)	***T (K)***	***P (atm)***	[a] ***[OH]***	[b] k_{OH}^{ETH}	[b] k_{OH}^{TFE}	[b] k_{OH}^{TCE}	[c] τ_{ETH}	[c] τ_{TFE}	[c] τ_{TCE}
0	290.2	0.999	3.0×10^{6}	7.55×10^{-12}	7.11×10^{-12}	2.26×10^{-12}	3.05	3.23	10.17
5	250.5	0.489	1.0×10^{6}	8.52×10^{-12}	8.24×10^{-12}	2.40×10^{-12}	1.01	1.05	3.59
10	215.6	0.239	5.7×10^{5}	9.91×10^{-12}	1.01×10^{-11}	2.55×10^{-12}	0.27	0.27	1.06
15	198.0	0.117	4.2×10^{5}	1.08×10^{-12}	1.16×10^{-11}	2.73×10^{-12}	1.19	0.11	0.47
20	208.0	0.057	3.7×10^{5}	9.68×10^{-12}	1.06×10^{-11}	2.62×10^{-12}	0.21	0.19	0.76
25	216.1	0.028	6.6×10^{5}	8.46×10^{-12}	1.00×10^{-11}	2.56×10^{-12}	0.33	0.28	1.08
30	221.5	0.014	1.6×10^{6}	7.10×10^{-12}	9.72×10^{-12}	2.50×10^{-12}	0.47	0.35	1.35
35	228.1	0.007	3.7×10^{6}	5.57×10^{-12}	9.34×10^{-12}	2.47×10^{-12}	0.77	0.46	1.73
40	240.5	0.003	6.8×10^{6}	3.86×10^{-12}	8.72×10^{-12}	2.39×10^{-12}	1.66	0.73	2.68
45	251.9	0.002	8.5×10^{6}	2.44×10^{-12}	8.21×10^{-12}	2.35×10^{-12}	3.68	1.09	3.82
50	253.7	0.001	6.8×10^{6}	1.59×10^{-12}	8.15×10^{-12}	2.34×10^{-12}	5.93	1.16	4.03

[a] units in molecules cm^{-3} as taken from ref. 91; [b] units in cm^3 $molecule^{-1}$ s^{-1}; [c] units in hours.

While the concentration of OH radicals is variable, depending on the exact location, solar flux and the mixing ratios of other gases, the suggested average value in the lower troposphere is 1.0×10^{6} molecules per cm^3. At this abundance, the atmospheric lifetimes here derived for CH_2=CH_2, CF_2=CHF and CCl_2=CHCl are 1.0, 1.1 and 3.6 days, in good agreement with those listed in the 2022 World Meteorological Organization ozone assessment report (1.7, 1.6 and 5.6 days, respectively). [92] Inspection of Table 3, reveals a different trend with the altitude of ethylene on the one side and the two halogenated olefins on the other, as also illustrated in Figure 12. Indeed, for the latter ones, the atmospheric lifetimes tend to shorten

moving from the ground level up to about 15 km, and then start to increase reaching a sort of plateau at about 45 km. At variance, as consequence of the pressure dependence of the rate constants, the atmospheric lifetimes of ethylene are characterized by a local maximum at the tropopause (c.a. 15 km), a smooth increase from 20 to 35 km and then a rapid raise that make this molecule to be the most long lived among the three olefins at an altitude of 50 km. Finally, it has to be noted that the global warming capacity of hydro-fluorocarbons have recently prompted the transition to the so-called very short-lived substances (VSLS), which are molecules with atmospheric lifetimes ranging from a few days to a few weeks. Despite the reduced residence time in the atmosphere, it has been pointed out that about 10% of a VSLS with an atmospheric lifetime of 1 week emitted to the tropical boundary layer can survive transport to the stratosphere. [93] In this respect, CCl_2=CHCl with a ground level atmospheric lifetime of about 10 days (which is probably underestimated to some extent) is a potential source of stratospheric Cl radicals, which are mainly produced through its OH degradation, and hence it may contribute to ozone depletion.

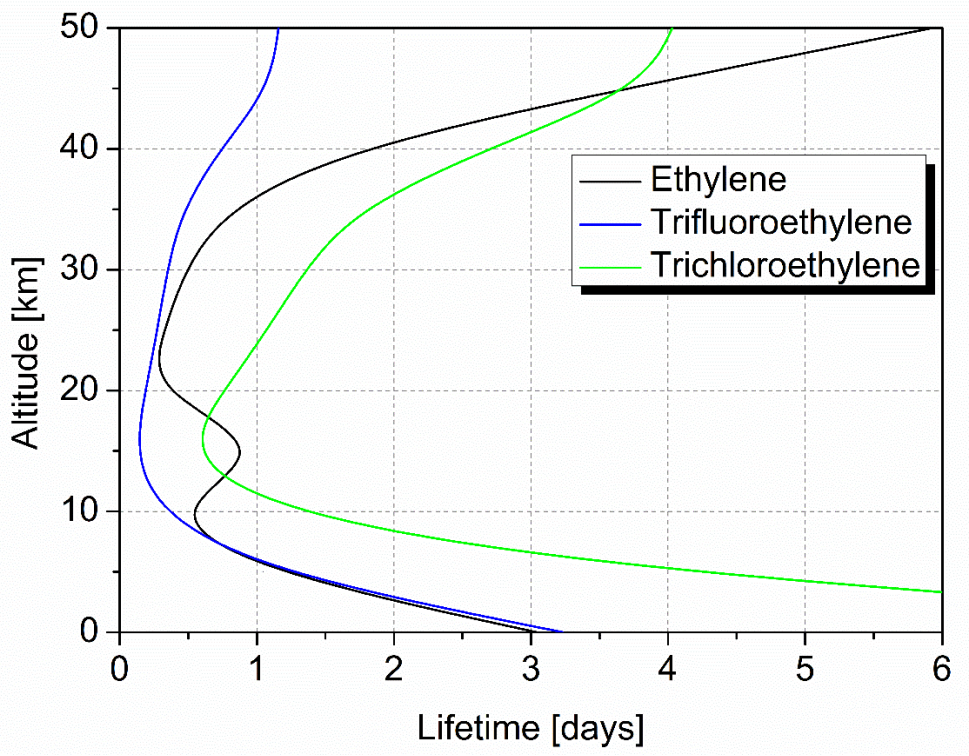

Figure 12. Trend of the atmospheric lifetimes of CH_2=CH_2, CF_2=CHF and CCl_2=CHCl with the atmospheric altitude. The computed points have been interpolated with a spline curve for better visualization.

4. Conclusions

In this study, we applied an effective yet reliable computational strategy for predicting accurately the OH atmospheric reactivity of olefins, focusing on the OH-initiated oxidative degradation of CH_2=CH_2, CF_2=CHF and CCl_2=CHCl. Optimized geometries of the entire set of species present in the corresponding potential energy surfaces were obtained at the rev-DSD-PBEP86-D3(BJ)/jun-cc-pV(T+*d*)Z level of theory, and their energetic properties were further refined by the parameter-free jChS composite model. Temperature and pressure dependent rate coefficients and product distributions at different atmospheric conditions were calculated within the RRKM/ME framework, where the state-of-the-art VRC-VTST combined with the two TS model was employed to treat barrierless channels. The computational protocol was first applied to the reaction of ethylene with the OH radical that, being thoroughly studied experimentally and theoretically in the literature, served as a case study to validate the methodology and assess its accuracy. An excellent agreement with the most recent experimental data was found, both regarding rate coefficient values (factor < 1.5) and temperature dependence, thus paving the way for the elucidation of the OH-reaction with the other two less studied halogenated olefins. Moreover, it was found that apart from the dominance of 2-hydroxyethyl radical adduct stabilization over the whole temperature range, a competition between the formation of vinyl alcohol and formaldehyde can occur at the lower temperature of 220 K, an observation not previously reported in the literature.

Regarding trifluoroethylene, it was observed that below 350 K, the principal pathway involves electrophilic π-addition to the–CF_2 site, but by 400 K, the addition to the –CHF group becomes the dominant one. Contrary to previous studies, the prevailing reaction channels at temperatures above 450 K for TFE were found to be the HF-eliminations from the initially formed hydroxyl-fluoroalkyl adduct radicals $CHFCF_2OH$ and CF_2CHFOH, to give the corresponding fluoroacetyl fluoride radicals. Additionally, formaldehyde and trifluoromethyl radical, also not reported in previous literature studies, have been identified as both thermodynamically and kinetically viable exit channels for this reaction. In the case of trichloroethylene, conclusive evidence on the fact that Cl-elimination channels dominate over adduct stabilization reaction at atmospheric temperatures was provided, verifying for the first time previous experimental observations by theoretical methodologies. At higher temperatures, other important key processes such as HCl removal or formation of formyl chloride (CHClO) and phosgene (CCl_2O), confirmed and summarized previous experimental and theoretical works.

While ethylene reactivity is not only temperature but also pressure-dependent, in the case of TFE and TCE rate constants are affected only by temperature. The substitution of hydrogen with fluorine minimally impacts the global rate constant for the reaction against the OH radical, whereas replacement with chlorine results in a roughly threefold reduction in the rate constant, mainly due to the inductive effects associated with the Cl atoms. The H-abstraction channels for the halogenated olefins appear too slow to compete with addition pathways at the temperatures investigated, and for that reason this route can play a moderate role only in the case of ethylene. Moreover, it was found that all three olefins exhibited a swift from negative to positive temperature dependence, varying from 450 K for ETH and TFE to 300 K for TCE. This trend was mainly attributed to the change in dominance of the two competing (outer and inner) transition states, that consequently affected the corresponding activation energies.

Finally, the computed rate constants for the reactions involving CX_2=CHX (X = H, F, and Cl) + OH, were utilized to determine the atmospheric lifetimes (τ) of the three olefins under study at various altitudes (h) in the atmosphere, since they are dependent of pressure (P), temperature (T) and [OH] concentration. It was shown that, for the halogenated olefins the τ generally decreases as one ascends from ground level up to approximately 15 km, whereas the τ of ethylene presented a rapid increase after that altitude, making it the most long-lived olefin of the three in the atmosphere. By using the suggested average [OH] value in the lower troposphere, the atmospheric lifetimes derived for ETH, TFE and TCE were found in good agreement with the ones reported in the recent 2022 World Meteorological Organization ozone assessment report.

DATA AVAILABILITY

The data supporting this article have been included as part of the ESI.

CONFLICTS OF INTEREST

There are no conflicts to declare.

ACKNOWLEDGMENTS

The authors would like to thank the STARK group for providing high-performance computing facilities and Scuola Normale Superiore for financial support through the project "Computational Modeling for Environmental Chemistry and Sustainability: from atmospheric monitoring to photo-catalysis". The research of NR has been performed during and with the

support of the Italian inter-university Ph.D. course in sustainable development and climate change (link: www.phd-sdc.it). The authors thank Vincenzo Barone (INSTM) for useful discussions and comments.

REFERENCES

1 D. Downie, The Vienna Convention, Montreal Protocol and Global Policy to Protect Stratospheric Ozone; Taylor & Francis: Oxford, 2012.
2 M. J. Molina and F. S. Rowland, *Nature*, 1974, **249**, 810–812.
3 P. W. Barnes, C. E. Williamson, R. M. Lucas, S. A. Robinson, S. Madronich, N. D. Paul, J. F. Bornman, A. F. Bais, B. Sulzberger, S. R. Wilson, A. L. Andrady, R. L. McKenzie, P. J. Neale, A. T. Austin, G. H. Bernhard, K. R. Solomon, R. E. Neale, P. J. Young, M. Norval, L. E. Rhodes, S. Hylander, K. C. Rose, J. Longstreth, P. J. Aucamp, C. L. Ballaré, R. M. Cory, S. D. Flint, F. R. de Gruijl, D.-P. Häder, A. M. Heikkilä, M. A. K. Jansen, K. K. Pandey, T. M. Robson, C. A. Sinclair, S.-Å. Wängberg, R. C. Worrest, S. Yazar, A. R. Young and R. G. Zepp, *Nat Sustain*, 2019, **2**, 569–579.
4 A. Mamantov, *Progress in Reaction Kinetics and Mechanism*, 2017, **42**, 307–333.
5 J. B. Burkholder, R. A. Cox and A. R. Ravishankara, *Chem. Rev.*, 2015, **115**, 3704–3759.
6 J. Reis, E. Benbrick, V. Bonneterre and P. S. Spencer, *Rev Neurol (Paris)*, 2016, **172**, 761–765.
7 E. R. Dorsey, M. Zafar, S. E. Lettenberger, M. E. Pawlik, D. Kinel, M. Frissen, R. B. Schneider, K. Kieburtz, C. M. Tanner, B. R. De Miranda, S. M. Goldman and B. R. Bloem, *J Parkinsons Dis*, 2023, **13**, 203–218.
8 L. Nolan, A.-L. Guihur, M. Manning and H. Sidebottom, in *Environmental Simulation Chambers: Application to Atmospheric Chemical Processes*, eds. I. Barnes and K. J. Rudzinski, Springer Netherlands, Dordrecht, 2006, pp. 171–179.
9 E. C. Tuazon, R. Atkinson, S. M. Aschmann, M. A. Goodman and A. M. Winer, *International Journal of Chemical Kinetics*, 1988, **20**, 241–265.
10 C. J. Christiansen and J. S. Francisco, *J. Phys. Chem. A*, 2010, **114**, 9163–9176.
11 L. A. B. Tichenor, A. J. Lozada-Ruiz, T. Yamada, Abdulazizel-Sinawi, P. H. Taylor, J. Peng, X. Hu and P. Marshill, *Proceedings of the Combustion Institute*, 2000, **28**, 1495–1502.
12 M. Hashimoto, T. Otsuka, M. Fukushima, H. Okamoto, H. Hayamizu, K. Ueno and R. Akasaka, *Science and Technology for the Built Environment*, 2019, **25**, 1–10.
13 Y. Higashi and R. Akasaka, .
14 L. Chen, T. Uchimaru, S. Kutsuna, K. Tokuhashi and A. Sekiya, *International Journal of Chemical Kinetics*, 2010, **42**, 619–628.
15 M. Baasandorj and J. B. Burkholder, *International Journal of Chemical Kinetics*, 2016, **48**, 714–723.
16 K. Tokuhashi, K. Takizawa and S. Kondo, *J. Phys. Chem. A*, 2018, **122**, 4593–4600.
17 S. Snitsiriwat, S. Yommee and J. W. Bozzelli, *J. Phys. Chem. A*, 2021, **125**, 5375–5384.
18 N. Tasinato, A. Pietropolli Charmet, G. Ceselin, Z. Salta and P. Stoppa, *J. Phys. Chem. A*, 2022, **126**, 5328–5342.
19 S. Snitsiriwat, S. Yommee and J. W. Bozzelli, *J. Phys. Chem. A*, 2019, **123**, 8017–8027.
20 V. L. Orkin, F. Louis, R. E. Huie and M. J. Kurylo, *J. Phys. Chem. A*, 2002, **106**, 10195–10199.
21 N. Tasinato, *International Journal of Quantum Chemistry*, 2014, **114**, 1472–1485.
22 E. Martínez-Núñez, G. L. Barnes, D. R. Glowacki, S. Kopec, D. Peláez, A. Rodríguez, R. Rodríguez-Fernández, R. J. Shannon, J. J. P. Stewart, P. G. Tahoces and S. A. Vazquez, *J Comput Chem*, 2021, **42**, 2036–2048.
23 E. Martínez-Núñez, *J Comput Chem*, 2015, **36**, 222–234.
24 E. Martínez-Núñez, *Phys. Chem. Chem. Phys.*, 2015, **17**, 14912–14921.
25 C. Puzzarini, J. Bloino, N. Tasinato and V. Barone, *Chem. Rev.*, 2019, **119**, 8131–8191.

26 R. Boussessi, G. Ceselin, N. Tasinato and V. Barone, *Journal of Molecular Structure*, 2020, **1208**, 127886.
27 G. Santra, N. Sylvetsky and J. M. L. Martin, *J. Phys. Chem. A*, 2019, **123**, 5129–5143.
28 S. Grimme, S. Ehrlich and L. Goerigk, *Journal of Computational Chemistry*, 2011, **32**, 1456–1465.
29 D. G. A. Smith, L. A. Burns, K. Patkowski and C. D. Sherrill, *J. Phys. Chem. Lett.*, 2016, **7**, 2197–2203.
30 E. Papajak, J. Zheng, X. Xu, H. R. Leverentz and D. G. Truhlar, *J. Chem. Theory Comput.*, 2011, **7**, 3027–3034.
31 G. Ceselin, V. Barone and N. Tasinato, *J. Chem. Theory Comput.*, 2021, **17**, 7290–7311.
32 A. Pietropolli Charmet, G. Ceselin, P. Stoppa and N. Tasinato, *Molecules*, 2022, **27**, 748.
33 V. Barone, G. Ceselin, F. Lazzari and N. Tasinato, *J. Phys. Chem. A*, 2023, **127**, 5183–5192.
34 S. Alessandrini, V. Barone and C. Puzzarini, *J. Chem. Theory Comput.*, 2020, **16**, 988–1006.
35 V. Barone, J. Lupi, Z. Salta and N. Tasinato, *J. Chem. Theory Comput.*, 2021, **17**, 4913–4928.
36 N. Rais, Z. Salta and N. Tasinato, *ACS Earth Space Chem.*, 2023, **7**, 892–900.
37 C. Baiano, J. Lupi, V. Barone and N. Tasinato, *J. Chem. Theory Comput.*, 2022, **18**, 3111–3121.
38 Z. Salta, N. Tasinato, J. F. Liebman and O. N. Ventura, *Chemical Thermodynamics and Thermal Analysis*, 2023, **12**, 100121.
39 O. N. Ventura, M. Segovia, M. Vega-Teijido, A. Katz, M. Kieninger, N. Tasinato and Z. Salta, *J. Phys. Chem. A*, 2022, **126**, 6091–6109.
40 Z. Salta, M. Vega-Teijido, A. Katz, N. Tasinato, V. Barone and O. N. Ventura, *Journal of Computational Chemistry*, 2022, **43**, 1420–1433.
41 T. Helgaker, W. Klopper, H. Koch and J. Noga, *J. Chem. Phys.*, 1997, **106**, 9639–9646.
42 Chr. Møller and M. S. Plesset, *Phys. Rev.*, 1934, **46**, 618–622.
43 J. J. P. Stewart, *J Mol Model*, 2013, **19**, 1–32.
44 MOPAC2016, James J. P. Stewart, Stewart Computational Chemistry, Colorado Springs, CO, USA, HTTP://OpenMOPAC.net (2016)
45 M. J. Frisch, G. W. Trucks, H. B. Schlegel, G. E. Scuseria, M. A. Robb, J. R.Cheeseman, G.Scalmani, V.Barone, G. A. Petersson and H. Nakatsuji, et al., Gaussian 16 Rev. C.01, Wallingford, CT, 2016.
46 H.-J. Werner, P. J. Knowles, G. Knizia, F. R. Manby and M. Schütz, *WIREs Comput Mol Sci*, 2012, **2**, 242–253.
47 J. Troe, *Faraday Trans.*, 1994, **90**, 2303.
48 E. E. Greenwald, S. W. North, Y. Georgievskii and S. J. Klippenstein, *J Phys Chem A*, 2005, **109**, 6031–6044.
49 Y. Georgievskii and S. J. Klippenstein, *J. Phys. Chem. A*, 2007, **111**, 3802–3811.
50 Y. Georgievskii and S. J. Klippenstein, *J. Chem. Phys.*, 2003, **118**, 5442–5455.
51 Y. Georgievskii and S. J. Klippenstein, *J. Phys. Chem. A*, 2003, **107**, 9776–9781.
52 Y. Zhao and D. G. Truhlar, *J. Chem. Theory Comput.*, 2008, **4**, 1849–1868.
53 B. J. Lynch, Y. Zhao and D. G. Truhlar, *J. Phys. Chem. A*, 2003, **107**, 1384–1388.
54 D. G. Truhlar and B. C. Garrett, *Acc. Chem. Res.*, 1980, **13**, 440–448.
55 B. Long, J. L. Bao and D. G. Truhlar, *J. Am. Chem. Soc.*, 2016, **138**, 14409–14422.
56 B. Long, Y. Xia and D. G. Truhlar, *J. Am. Chem. Soc.*, 2022, **144**, 19910–19920.
57 J. Zheng and D. G. Truhlar, *J. Chem. Theory Comput.*, 2013, **9**, 1356–1367.
58 J. Bloino, M. Biczysko and V. Barone, *J. Chem. Theory Comput.*, 2012, **8**, 1015–1036.
59 J. Zheng, J. L. Bao, R. Meana-Pañeda, S. Zhang, B. J. Lynch, J. C. Corchado, Y.-Y. Chuang, P. L. Fast, W.-P. Hu, Y.-P. Liu, G. C. Lynch, K. A. Nguyen, C. F. Jackels, A. Fernandez Ramos, B. A. Ellingson, V. S. Melissas, J. Villà, I. Rossi, E. L. Coitiño, J. Pu, T. V. Albu, A. Ratkiewicz, R. Steckler, B. C. Garrett, A. D. Isaacson, and D. G. Truhlar, Polyrate-version 2017-C (University of Minnesota, Minneapolis, MN, 2017).
60 J. Zheng, J. L. Bao, S. Zhang, J. C. Corchado, R. Meana-Pañeda, Y.-Y. Chuang, E. L. Coitiño, B. A. Ellingson, and D. G. Truhlar, Gaussrate 17 (University of Minnesota, Minneapolis, MN, 2017).
61 Y. Georgievskii, J. A. Miller, M. P. Burke and S. J. Klippenstein, *J. Phys. Chem. A*, 2013, **117**, 12146–12154.
62 C. Eckart, *Phys. Rev.*, 1930, **35**, 1303–1309.

63 M. S. Johnson, X. Dong, A. Grinberg Dana, Y. Chung, D. Jr. Farina, R. J. Gillis, M. Liu, N. W. Yee, K. Blondal, E. Mazeau, C. A. Grambow, A. M. Payne, K. A. Spiekermann, H.-W. Pang, C. F. Goldsmith, R. H. West and W. H. Green, *J. Chem. Inf. Model.*, 2022, **62**, 4906–4915.
64 P. A. Cleary, M. T. B. Romero, M. A. Blitz, D. E. Heard, M. J. Pilling, P. W. Seakins and L. Wang, *Phys. Chem. Chem. Phys.*, 2006, **8**, 5633–5642.
65 A. B. Vakhtin, J. E. Murphy and S. R. Leone, *J. Phys. Chem. A*, 2003, **107**, 10055–10062.
66 D. Fulle, H. f. Hamann, H. Hippler and C. p. Jänsch, *Berichte der Bunsengesellschaft für physikalische Chemie*, 1997, **101**, 1433–1442.
67 T. Klein, I. Barnes, K. H. Becker, E. H. Fink and F. Zabel, *J. Phys. Chem.*, 1984, **88**, 5020–5025.
68 K. H. Becker, H. Geiger and P. Weisen, *Chemical Physics Letters*, 1991, **184**, 256–261.
69 J. P. A. Lockhart, E. C. Gross, T. J. Sears and G. E. Hall, *International Journal of Chemical Kinetics*, 2019, **51**, 412–421.
70 J. P. Senosiain, S. J. Klippenstein and J. A. Miller, *J. Phys. Chem. A*, 2006, **110**, 6960–6970.
71 D. M. Golden, *J. Phys. Chem. A*, 2012, **116**, 4259–4266.
72 M. Akbar Ali and J. R. Barker, *J. Phys. Chem. A*, 2015, **119**, 7578–7592.
73 P. Liang, E. V. F. de Aragão, L. Giani, L. Mancini, G. Pannacci, D. Marchione, G. Vanuzzo, N. Faginas-Lago, M. Rosi, D. Skouteris, P. Casavecchia and N. Balucani, *J. Phys. Chem. A*, 2023, **127**, 4609–4623.
74 D. J. Medeiros, S. H. Robertson, M. A. Blitz and P. W. Seakins, *J. Phys. Chem. A*, 2020, **124**, 4015–4024.
75 C. Xu, C. Wang, B. Li, L. Hu and F. L. Gu, *Phys. Chem. Chem. Phys.*, 2019, **21**, 1367–1374.
76 M. Balaganesh and B. Rajakumar, *J. Phys. Chem. A*, 2012, **116**, 9832–9842.
77 M. Baasandorj, P. Marshall, R. L. Waterland, A. R. Ravishankara and J. B. Burkholder, *J. Phys. Chem. A*, 2018, **122**, 4635–4646.
78 U. P. Kakati, D. Dowerah, R. C. Deka, N. K. Gour and S. Paul, *ACS Earth Space Chem.*, 2023, **7**, 501–514.
79 K. Kirchner, D. Helf, P. Ott and S. Vogt, *Berichte der Bunsengesellschaft für physikalische Chemie*, 1990, **94**, 77–83.
80 E. O. Edney, T. E. Kleindienst and E. W. Corse, *International Journal of Chemical Kinetics*, 1986, **18**, 1355–1371.
81 W. Klopffer, R. Frank, E. Kohl and F. Haag, Chemiker-Zeitung, 1986, **110**, 57-61.
82 J. S. Chang and F. Kaufman, *The Journal of Chemical Physics*, 1977, **66**, 4989–4994.
83 C. J. Howard, *Journal of Chemical Physics*, 1976, **65**, 4771–4777.
84 R. Atkinson, D. L. Baulch, R. A. Cox, J. N. Crowley and R. F. Hampson, .
85 J. M. Tedder, *Angewandte Chemie International Edition in English*, 1982, **21**, 401–410.
86 B. Giese, *Angewandte Chemie International Edition in English*, 1983, **22**, 753–764.
87 R. Naaman and Z. Vager, Eds., Springer US, Boston, MA, 1988.
88 M. J. Kurylo and V. L. Orkin, *Chem. Rev.*, 2003, **103**, 5049–5076.
89 M. Prather and C. M. Spivakovsky, *Journal of Geophysical Research: Atmospheres*, 1990, **95**, 18723–18729.
90 M. J. Rossi, D. F. McMillen and D. M. Golden, *J. Phys. Chem.*, 1984, **88**, 5031–5039.
91 G. Brasseur and S. Solomon, *Aeronomy of the Middle Atmosphere: Chemistry and Physics of the Stratosphere and Mesosphere*, 2005.
92 N. C. S. Laboratory (CSL), NOAA CSL, https://csl.noaa.gov/assessments/ozone/2022/.
93 J. G. Levine, P. Braesicke, N. R. P. Harris, N. H. Savage and J. A. Pyle, *Journal of Geophysical Research (Atmospheres)*, 2007, **112**, D04308.